*ChemElectroChem*

Chemistry Europe
European Chemical Societies Publishing

ChemElectroChem

RESEARCH ARTICLE OPEN ACCESS

# Hierarchically Structured Potassium Titanium Phosphates as Reference and Diagnostic Electrodes in Potassium-Ion Batteries

Andreas Heyn | Joshua A. Psille | Iurii Panasenko | Holger Geßwein | Monika Raab | Joachim R. Binder | Fabian Jeschull

Institute for Applied Materials, Karlsruhe Institute of Technology (KIT), Eggenstein-Leopoldshafen, Germany

**Correspondence:** Fabian Jeschull (fabian.jeschull@kit.edu)

**Received:** 7 July 2026 | **Revised:** 7 August 2026 | **Accepted:** 13 August 2026

**Keywords:** diagnostic electrodes | hierarchical structures | microstructure | potassium titanium phosphates (KTP, KTPO) | potassium-ion-batteries | reference electrodes

## ABSTRACT

The high reactivity and unstable potential of metallic potassium limits its application as a stable reference or counter electrode for a precise and reliable electrochemical characterization of electrode active materials for potassium-ion batteries (PIBs). In this study, we investigate the application of hierarchically structured $KTi_2(PO_4)_3$/C (KTP/C) and $KTiOPO_4$/C (KTPO/C) composites as a reference (RE) or diagnostic electrode (DE) respectively. KTP/C is a promising RE due to its stable potential at 1.88 V versus $K^+$/K on a long-term scale for more than 250 h in a three-electrode configuration with a KTP/C working electrode (WE) and RE against a metallic potassium counter electrode (CE). Instead, KTPO/C exhibits a low kinetic limitation, making this material ideally suited as a DE for PIBs. To prove the suitability of KTPO/C as a DE, a full-cell setup of $K_3V_2(PO_4)_3$/C (KVP/C) as WE against a KTPO/C DE was developed. The full-cell setup with a KTPO/C DE revealed a significant underestimation of the properties of KVP/C compared to the conventional half-cell setups with a metallic potassium CE. The developed RE and DE for PIBs facilitate an accurate and reliable electrochemical characterization of electrode active materials for and will accelerate the future development of PIBs.

## 1 | Introduction

With lithium-ion batteries (LIBs) predicted to have a market share of 90% in the future, there is an increasing need for alternative battery technologies with less dependency on critical minerals like cobalt or nickel [1, 2]. Sodium-ion batteries (SIBs) and the latest addition to the monovalent ion portfolio, potassium-ion batteries (PIBs), provide two technologies that can compete and complement LIBs. SIBs and PIBs are potentially cheaper and more sustainable, because they rely on a more abundant mineral basis and avoid critical elements [3]. As sodium and potassium both do not form alloys with aluminum, its allows its use as current collector for negative electrodes instead of expensive copper used in LIBs [4]. Besides the higher working voltages due to the lower alkali metal potential, there is one main advantage of PIBs over SIBs: Potassium ions can reversibly intercalate into graphite, which means that anode production is already possible on large scale for PIBs [5, 6]. Based on these facts, the main critical research fronts for PIBs arise: development of suitable high-voltage cathode materials and electrolytes compatible with graphite [4, 7].

For the development and optimization of advanced cathode materials and electrolytes for PIBs, precise and reliable electrochemical characterization methods are inevitable [7–9]. Traditionally, most of the electrochemical characterizations for

alkali-ion batteries are done in a so-called "half-cell" setup, where a metallic counter electrode (CE) is utilized to study, for example, the insertion characteristics of an electrode material as the working electrode (WE) [9–12]. Several previous studies outlined that a major problem in postlithium systems, but for PIBs especially, are interferences from the metallic potassium CE when characterizing electrode materials or electrolytes in a half-cell setup. The problems are associated with [9, 12–15]

1. High resistivity of potassium metal itself leads to increased cell polarization,
2. Growth of mossy structures and dendrites at the potassium metal surface and
3. Severe crosstalk and self-discharge processes, and
4. Rapid accumulation of parasitic electrolyte degradation products.

A main problem is the poor passivation of the potassium metal surface from recurrent electrolyte degradation processes. This could amplify resistive surface layer growth and foster accumulation of parasitic, soluble electrolyte degradation products that may induce crosstalk processes [9, 15]. In addition, the potassium metal CE builds up high resistivity and polarization during cycling, leading to an increased bias on the C-rate capability test and cycle life assessment of different electrode materials in half-cell setups [3, 9, 12–16].

Therefore, any source of metallic potassium can massively influence the characterization of electrode materials and could lead to underestimated material performance [3, 7–9]. More reliable electrochemical characterization thus require three-electrode setups with stable reference electrodes (RE). REs are defined as (electro)chemically inert materials, with a well-defined redox reaction that generates a stable potential reading over extended time intervals (typical drift rates are below 1 mV/h). Ideally, they exhibit fast electrode kinetics, so they stay nonpolarizable even if a current is applied. It is further beneficial if the RE operates within the stability window of the electrolyte to avoid recurrent side reactions [7, 9, 10]. Previous examples for PIBs include pretreated potassium electrodes [8], K–In or K–Bi alloys [7], or Ag/AgCl references [9]. A direction that was not explored so far for PIBs are insertion-type REs, where flat sections in the voltage profile (plateaus) mark points with stable equilibrium potentials suitable as point of reference [10]. In LIBs, $LiFePO_4$ (LFP) [17] and $Li_4Ti_5O_{12}$ (LTO) [18] are well-known examples for this application. Strong contenders for this purpose are materials within the class of polyanionic titanium phosphates. The NASICON-type $KTi_2(PO_4)_3$ (KTP) could be a promising CE for PIBs as it possesses a well-defined voltage profile between 1.6 and 1.9 V low volume change during cycling (11.7%), indicating its structural stability [19] and good $K^+$ diffusion with ionic conductivities up to $10^{-12}$ $cm^2$ $s^{-1}$ [20, 21].

For truly alkali-metal-free cell setups, alternatives need to be developed for their common role as CEs. A recent example by Hwang et al. is the use of NASICON-type sodium titanium phosphate ($NaTi_2(PO_4)_3$) as CEs instead of sodium to reduce parasitic side reactions at the reactive sodium metal surface [22]. Similarly, graphite electrodes exhibit low operation potentials and significant degrees of irreversible side reactions that may give rise to crosstalk and rapid loss of potassium inventory. Following previous works by Dose et al. [23, 24], oversized LFP or LTO electrodes (i.e., high areal capacities for high N/P ratios) could replace more reactive CEs. As an oversized CE, they provide an excess charge carrier inventory and in their function as a quasi-RE, they exhibit a stable redox potential over a wide state-of-charge range owing to their flat voltage profile. Hence, the authors referred to this particular type of counter-RE as diagnostic electrode (DE). One such candidate for the PIB system could be the orthorhombic $KTiOPO_4$ (KTPO) with a well-defined plateau at around 1.1 V and a width of around 55 mAh $g^{-1}$ [25]. The very stable open 3D structure of the KTPO- material class with just 9.5% volume change during cycling [25] enables a fast $K^+$ diffusion with ionic conductivities of up to $10^{-10}$ $cm^2$ $s^{-1}$. This value is an order of magnitude higher than for NASICON structures and leads to low voltage hysteresis, indicating low kinetic limitations [25, 26].

Unfortunately, polyanionic materials intrinsically suffer from low electronic conductivity. To overcome polarization effects caused by low electronic conductivity, which could make a material unsuitable for its use as a RE or DE, strategies to enhance the electronic conductivity have to be applied. This could be done, for example, by nano-/microstructuring or in situ coating with conductive carbon layers [27–29].

In this study, we investigate the usability of KTP/C or KTPO/C composites as RE or DE in PIBs for the first time. Therefore, we developed an easily scalable solid-state approach combined with a spray-drying method to create hierarchically structured KTP/C- and KTPO/C-composites with improved electrochemical performance. The synthesis process of our recent publication [30] was transferred to the synthesis of KTP/C or KTPO/C with minor adjustments. We further prove their use as RE or DE, identifying KTP/C as the most promising RE and KTPO/C as DE for PIBs. This study reports the use of an insertion-type material as a RE or DE in PIBs for the first time and could improve precise electrochemical characterization for PIBs greatly.

## 2 | Results and Discussion

The KTP/C and KTPO/C samples were all synthesized via a solid-state reaction process combined with a spray-drying and sintering process according to our previous study on KVP/C composites [30]. The synthesis process is schematically shown in Figure 1. For KTP/C as carbon source, only β-lactose was added in process step 3 with 12.5 wt%. For KTPO/C, 7.5 wt% sucrose was added in process step 1 and 15 wt% β-lactose were added in step 3 as a carbon source.

### 2.1 | Synthesis of Hierarchically Structured KTP/C and KTPO/C Composites

#### *2.1.1 | KTP/C*

The phase evolution and crystallization behavior of KTP was studied via simultaneous thermal analysis coupled with evolved gas

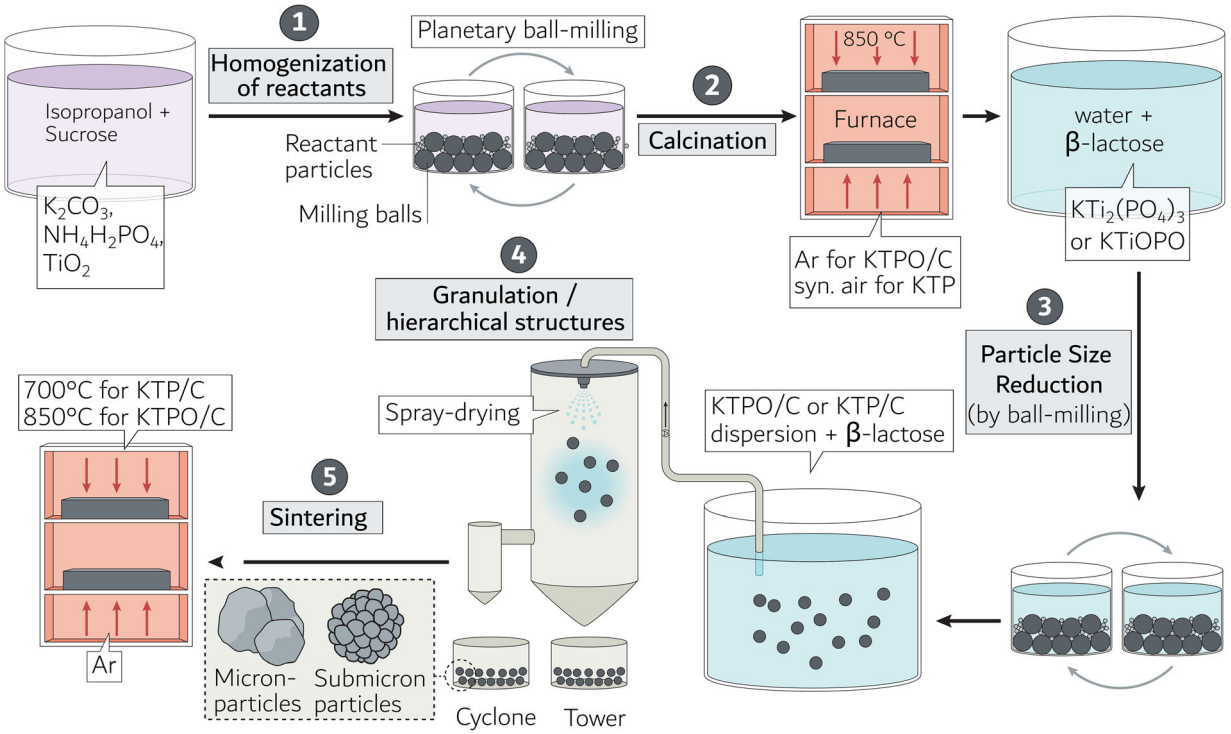


**FIGURE 1** | Schematic drawing of the synthesis process of hierarchically structured KTP/C- and KTPO/C-composites with: (1) Mixing of reactants by planetary ball-milling in isopropanol with subsequent drying, (2) calcination under argon (KTPO/C) or synthetic air (KTP) atmosphere in a chamber oven at 850 °C, (3) mixing and grinding of KTP or KTPO/C with β-lactose in water by planetary ball-milling, (4) spray-drying of the KTP or KTPO/C dispersion in water with β-lactose, and (5) sintering of hierarchically structured secondary KTP/C or KTPO/C particles under an argon atmosphere in a chamber oven at 700 °C for KTP/C and 850 °C for KTPO/C.

analysis via Fourier transform infrared spectroscopy (TG/FT-IR) under synthetic air, as shown in Figure 2a,b. In the top panel of Figure 2a, a continuous mass loss can be observed starting from 175 °C up to a temperature of 600 °C. The total mass loss accounted for about 20% and remained at this value until the upper temperature cut-off of 1000 °C was reached. The strong endothermic signal in the differential scanning calorimetry (DSC) signal coincides with the mass loss until around 600 °C and the release of the gaseous byproducts $NH_3$ and $H_2O$ (150–400 °C). This indicates the decomposition of the reactant $NH_4H_2PO_4$. $CO_2$ as a sensitive IR probe typically indicated the decomposition of $K_2CO_3$. In this synthesis, however, only a minor $CO_2$ signal at around 450 °C was detected, suggesting no significant $CO_2$ formation and the absence of $K_2CO_3$ in the precursor. This is likely because $K_2CO_3$ decomposes during the preparation of the precursor in 2-propanol in the first ball-milling step, probably under formation of KOH as the actual potassium source in the calcination reaction to KTP.

The decomposition of $K_2CO_3$ was confirmed by additional FT-IR measurements on the precursor (Figure S1). Instead, the presence of KOH in the precursor correlates well with the mass loss and prominent IR signal for water at elevated temperatures, indicating the decomposition of KOH. Beginning at around 750 °C and continuing until a temperature of 950 °C, a broad exothermic area is apparent in the DSC signal, indicating the crystallization of the KTP phase during the calcination reaction under synthetic air. Based on the thermal analysis and the assumption of KOH as potassium source, we propose the following reaction scheme (Equation (1)):

$$2\,KOH + 4\,TiO_2 + 6\,NH_4H_2PO_4 \xrightarrow{\text{syn.air},\Delta T} 2\,KTi_2(PO_4)_3 + 6\,NH_3 + 10\,H_2O \quad (1)$$

Based on the results of the thermal analysis, a reaction temperature 850 °C under synthetic air was found to be optimal. Inductive-coupled plasma optical emission spectroscopy (ICP-OES) analysis on pure KTP sample revealed a K:Ti:P-ratio of 1.0:1.87:2.88, which indicates a minor Ti-deficiency. On the contrary, X-ray diffraction (XRD) analysis of the pure KTP sample revealed phase purity without any impurity visible in the powder XRD pattern (Figure S2). Sharp reflexes and low background of the XRD pattern indicate high crystallinity of the KTP phase, while the crystallite size was estimated with 81 (2) nm.

A theoretical reaction yield of around 75% was expected according to Equation (1), while a residual mass of 80% is obtained after the thermal analysis under synthetic air. The differences in the reaction yield could arise due to a starting decomposition reaction of $NH_4H_2PO_4$, leading to a release of $NH_3$ during precursor preparation by ball-milling in 2-propanol. Additionally, a reaction of the potassium source with $NH_4H_2PO_4$ during precursor preparation to $K_2HPO_4$ is possible. After preparation of the precursors, a typical smell of ammonia was obtained. This could result in fact in an increased reaction yield compared to theoretical expected reaction yield.

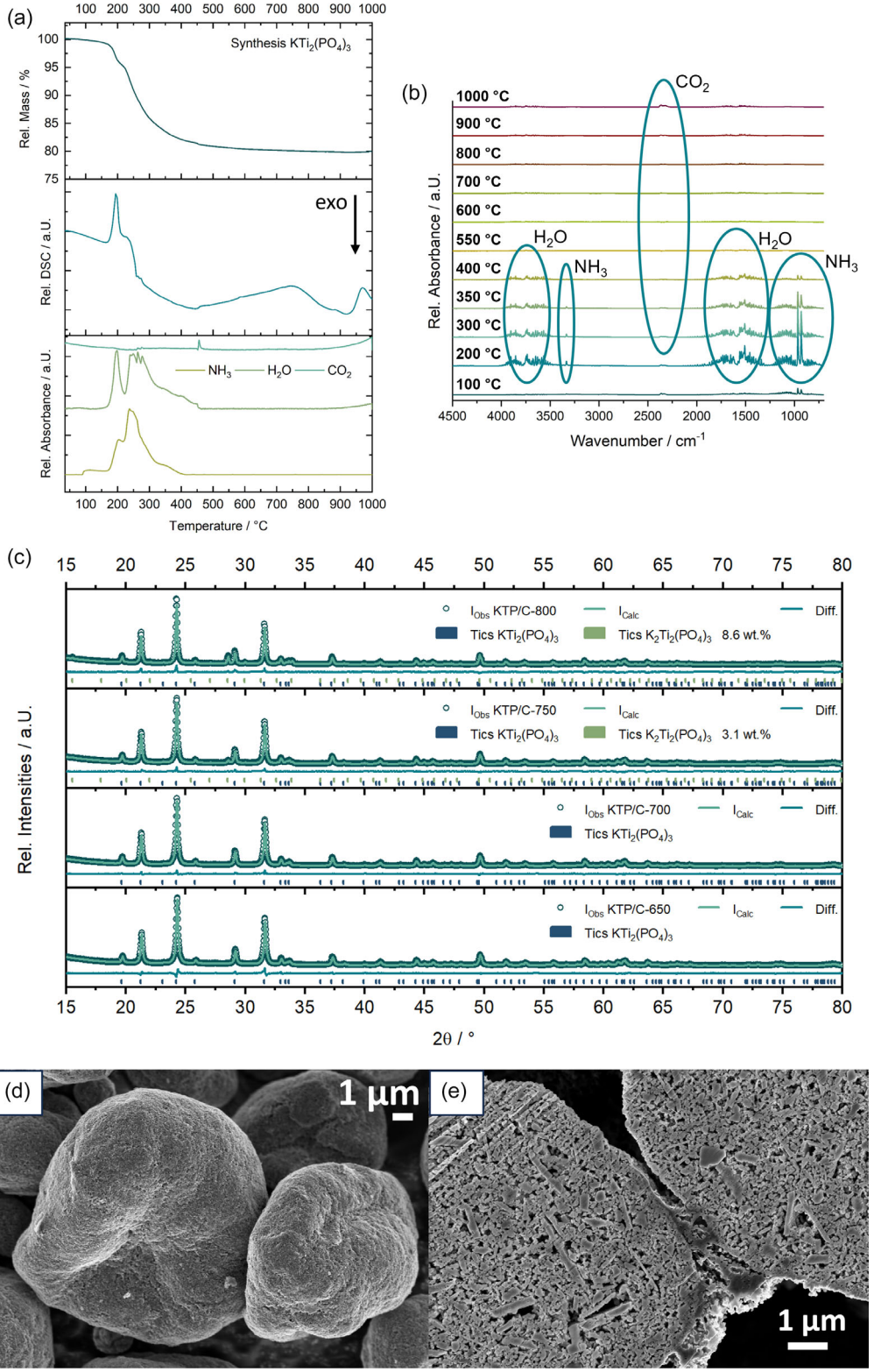


**FIGURE 2** | TG/DSC-IR-analysis on the calcination reaction of pure KTP under synthetic air (80% $O_2$/20% $N_2$) with (a) TGA (top), DSC (middle), IR traces of gaseous byproducts (bottom) and (b) FT-IR spectra at different temperatures with marked signals for main gaseous byproducts during the calcination reaction, (c) XRD analysis on KTP/C sintered at different temperatures with the performed Rietveld-refinement of the observed powder XRD-pattern against the rhombohedral structural model with the symmetry $R\bar{3}c$ of KTP (ICSD-67091 ICSD release 2025.1, Lunezheva et al. [31]) and the cubic structural model with the symmetry $P2_13$ of $K_2Ti_2(PO_4)_3$ (ICSD-202888 ICSD release 2025.1, Leclaire et al. [32]). SEM images of (d) the morphology and (e) the cross-sections of the KTP/C-700 composites after completion of the synthesis process.

To create hierarchically structured KTP/C composites, the pure KTP has to be spray-dried and sintered under an Ar atmosphere in the presence of a carbon source, in the case of this study, 12.5 wt% of β-lactose. The XRD analysis of KTP/C samples sintered at different temperatures is shown in Figure 2c. The Rietveld refinement on the diffraction patterns of the KTP/C samples against the structural model of the KTP phase (ICSD-67091, ICSD release 2025.1, Lunezheva et al. [31]) revealed increasing amounts of the cubic $K_2Ti_2(PO_4)_3$ phase (ICSD-202888, ICSD release 2025.1, Leclaire et al. [32]) with increasing sintering temperature up to 8.1 wt% in KTP/C-800. We assume that the presence of a carbon matrix/in situ carbon coating at temperatures up to 800 °C leads to a partwise reduction of $Ti^{+4}$ to $Ti^{+3}$ and the formation of the cubic $K_2Ti_2(PO_4)_3$ impurity phase. The phase analysis suggests an optimum sintering temperature around 700 °C under an Ar atmosphere (Figure 2c) to maintain phase purity of the KTP/C composites and maximize sintering activity at the same time. Compared to the pure KTP, the reflexes of the KTP/C-700 are broadened, while the crystallite size was estimated with 40 (1) nm, indicating nanocrystallinity. The necessary ball-milling and in situ carbon coating decrease the crystallinity of the KTP/C-700 compared to the pure KTP. Nevertheless, the refined lattice parameters of KTP/C-700 are in good agreement with literature [19, 31] (refined: $a = b = 8.3615(1)$ Å, $c = 23.1005(6)$ Å, $\alpha = \beta = 90°$, $\gamma = 120°$, $V = 1398.92$ Å$^3$).

All determined powder characteristics of KTP/C-700 and scanning electron microscopy (SEM) images are shown in Table 1 and Figure 2d,e. Nearly spherical-shaped KTP/C granules are obtained after spray-drying and sintering. Some grooves on the surface of the granules are visible, indicating a too low binder poly(acrylic acid)(PAA) or solid content to stabilize the spherical morphology (Figure 2d,e) [33]. The carbon content after completion of the synthesis process was determined to be 4.2 wt%, while a carbon content of 5.3 wt% is theoretically expected assuming a complete carbonization of the added β-lactose (Table 1). Differences could arise due to a partwise consumption of the formed carbon matrix for reduction of tiny amount of $Ti^{+4}$ to $Ti^{+3}$ or an incomplete carbonization of β-lactose. This could lead to the release of gaseous byproducts in form of lower molecular species like $CO_2$ or CO that could be formed during decomposition of the β-lactose, similar to that seen for the KVP/C synthesis at higher temperatures [30]. The cross-sections of the granules reveal an open intragranular porosity without any dense surface layer, which should be beneficial for the electrochemical performance of the KTP/C composites. In combination, the high specific surface (49.4 $m^2 g^{-1}$), the carbon coating and the open porosity (49.3%) with nanometer-sized pores create a unique microstructure, which improves the electronic conductivity and diffusion kinetics of the granules, as similarly seen in our previous work on KVP/C composites [30]. Electrochemical characterization of the hierarchically structured KTP/C and their utilization as an RE for PIBs will be discussed in Section 2.2.

### 2.1.2 | KTPO/C

In a similar fashion to the synthesis of KTP, the structural evolution and crystallization behavior of KTPO/C were studied via TG/DSC-IR analysis under an Ar atmosphere (Figure 3a,b).

Two distinct mass losses are observed in the TGA signal of the calcination reaction of KTPO/C. At temperatures between 100 and 300 °C, the mass loss correlates with a sharp endothermic signal in the DSC. This indicates the decomposition of the reactants $NH_4H_2PO_4$ and sucrose, which is confirmed by the IR traces of gaseous byproducts as the main peaks for $H_2O$, $NH_3$, and $CO_2$ are located at temperatures up to 300 °C. At a temperature between 600 and 650 °C, a strong exothermic signal in the DSC indicates the crystallization of the KTPO phase. Above 850 °C, another mass loss is apparent in the TGA. The mass loss correlates with a strong endothermic signal in the DSC and a release of CO instead of $CO_2$ in the IR traces. This could indicate the start of a decomposition reaction of the KTPO with formed carbon coating, leading to impurity phase formation as similar to that seen for NVP/C or KVP/C composites [30, 36]. All $CO_2$ signals in the IR traces are ascribed to the carbonization of sucrose. An additional $CO_2$ signal should be observed in the IR traces for the crystallization of the KTPO phase between 600 and 650 °C due to the reaction of $K_2CO_3$ with the other reactants of the precursor. However, as described for the KTP precursor above, FT-IR measurements on the KTPO/C precursor (Figure S1) confirmed the decomposition or reaction of $K_2CO_3$ with $NH_4H_2PO_4$ during precursor preparation via planetary ball milling in 2-propanol.

We propose the following reaction scheme for the calcination reaction of KTPO/C under an Ar atmosphere under the assumption $K_2CO_3$ converted to KOH (Equation (2)):

$$\begin{aligned} &KOH + TiO_2 + NH_4H_2PO_4 + nC_{12}H_{22}O_{11} \xrightarrow{Ar,\Delta T} \\ &\times KTiOPO_4/C_n + NH_3 + (11n+2)H_2O \end{aligned} \quad (2)$$

An 81% residual mass was obtained from thermal analysis under an Ar atmosphere, aligning with the theoretical yield of 76% after calcination, assuming complete carbonization of 7.5 wt% sucrose. Calcination and sintering temperature at 850 °C chosen in this work is at the upper end of the temperature corridor to produce the target compound. The higher yields found herein can be explained by the precursor preparation and associated chemical reactions during planetary ball milling in 2-propanol (i.e., prior to

**TABLE 1** | Summary of all relevant powder characteristics after completion of the synthesis process for the hierarchical structured KTP/C-700 and KTPO/C composites.

| Composite | Calcination temp., °C | Sintering temp., °C | C-content after sintering, wt% | Median secondary particle size, µm | Specific surface, $m^2 g^{-1}$ | Porosity, % | Pore size, nm |
|---|---|---|---|---|---|---|---|
| KTP/C-700 | 850 | 700 | 4.2 | 10.2 | 49.4 | 49.3 | 66 |
| KTPO/C | 850 | 850 | 5.2 | 11.7 | 27.7 | 39.8 | 42 |

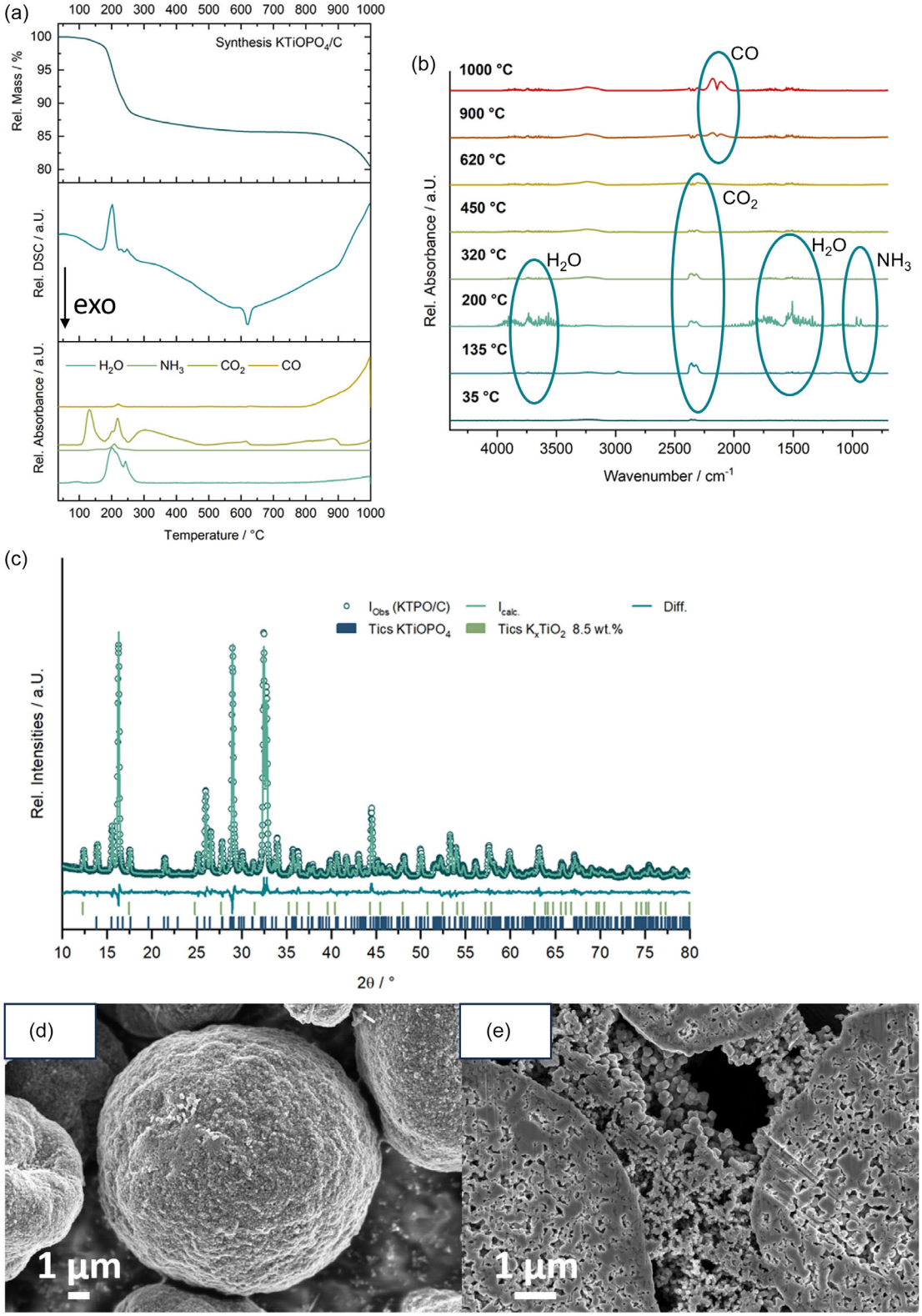


**FIGURE 3** | TG/DSC-IR-analysis on the calcination reaction of KTPO/C under Ar atmosphere with (a) TGA (top), DSC (middle), IR traces of gaseous byproducts (bottom) and (b) FT-IR spectra at different temperatures with marked signals for main gaseous byproducts during the calcination reaction, (c) XRD analysis on KTPO/C sintered at 850 °C with the performed Rietveld-refinement of the observed powder XRD-pattern against the orthorhombic structural model with the symmetry $Pna2_1$ of KTPO (ICSD-182657, ICSD release 2025.1, Norberg et al. [34]) and the tetragonal structural model with the symmetry I4/m of the hollandite type $K_xTiO_2$ (ICSD-247826, ICSD release 2025.1, Sakao et al. [35]), (d) morphology and (e) cross-sections of the KTPO/C granules after completion of the synthesis studied via SEM.

calcination), for example. partial decomposition of $K_2CO_3$ and $NH_4H_2PO_4$ occurs, releasing $CO_2$ and $NH_3$ (seen as low-intensity IR signal, as well as a characteristic ammonia odor). In addition, the potassium source and $NH_4H_2PO_4$ may form $K_2HPO_4$, which further contributes to the increased residual mass.

A theoretical carbon content of 3.2% would be expected, assuming complete carbonization of the 7.5 wt% sucrose during calcination. Experimentally, only a carbon content of 2.2% was determined for the KTPO/C after calcination. The addition of 15 wt% of β-lactose for the spray-drying and sintering process to create hierarchically structured KTPO/C composites should theoretically lead to an increase in carbon content of 6.3% assuming the complete carbonization of the β-lactose. Experimentally, a total carbon content of 5.2% for the hierarchically structured KTPO/C composites after completion of the synthesis process was determined, meaning an increase of only 3.0% carbon content due to the carbonization of the 15 wt% β-lactose. These differences could arise due to an incomplete carbonization of the two carbon sources sucrose and β-lactose during calcination and sintering, leading to the volatilization of lower molecular species like $CO_2$ or CO as determined via the thermal analysis at higher temperatures (Figure 3a,b) and/or the consumption of the formed carbon coating for the reduction of $Ti^{+4}$ to $Ti^{+3}$, leading to impurity phase formation. The carbothermal reduction of some $Ti^{+4}$ is confirmed by XRD and the performed Rietveld analysis, as shown in Figure 3c. The high calcination/sintering temperature of 850 °C and the presence of carbon leads to the impurity phase formation of about 8.5 wt% of the hollandite-type $K_xTiO_2$ bronze (symmetry I4/m) [35] after completion of the synthesis process of the KTPO/C composites. Additionally, ICP-OES analysis revealed a stochiometric ratio of K:Ti:P of 1:1.02:0.98, which could be seen as a further indication for the formation of a Ti-rich impurity. Nevertheless, a very good agreement between the calculated and recorded diffraction pattern is observed for the KTPO/C composites. The narrow reflexes indicate a high crystallinity, while the crystallite size was estimated as 50 (1) nm. The refined lattice parameters are in good agreement with literature (refined: $a = 12.8179(4)$ Å, $b = 6.4045(2)$ Å, $c = 10.5844(2)$ Å, $\alpha = \beta = \gamma = 90°$, and $V = 867.26$ Å$^3$) [26, 34, 37]. All relevant powder characteristics for the KTPO/C composites are summarized in Table 1.

Similar to the synthesis of the KTP/C and KVP/C [30] composites, nearly spherical-shaped granules of the KTPO/C composites (Figure 3d,e) with an open porosity of around 39.8% and a specific surface of 27.7 $m^2 g^{-1}$ were obtained. The cross-sections of the granules reveal an open porosity with just a small denser layer at the surface of the granules. The high specific surface, open porosity with nanometer-sized pores (median: 42 nm) and carbon coating create a unique microstructure, which should lead to improved electronic conductivity and diffusion kinetics. This could lead, in fact, to improved electrochemical properties, which will be discussed in the following sections for the KTP/C and KTPO/C composites.

## 2.2 | Electrochemical Evaluation of KTP/C and KTPO/C

Electrochemical evaluation of the KTP/C and KTPO/C composites was performed in CR2032-format potassium half-cells in a voltage window of 1.0–4.0 V. Galvanostatic cycling at various C-rates ranging from C/20 to 1C (1C = 128 mA $g^{-1}$) was performed to determine the basic electrochemical properties like maximum charge capacity, C-rate capability, and the location of the voltage plateau. In addition, both materials were subjected to a self-discharge test to evaluate their applicability as reference or DEs. As a negative electrode material, the cycling of KTP/C-700 and KTPO/C WEs starts with a reduction step (cathodic current). All stated capacities refer to the composite mass, including the carbon fraction, and not solely the active material mass.

### 2.2.1 | *KTP/C as Negative Electrode and RE*

*2.2.1.1 | KTP/C as Negative Electrode.* In Figure 4a, the voltage profiles of the C-rate capability test of the KTP/C-700 composite are shown. At C/20, the KTP/C-700 composite reached 125 mAh $g^{-1}$ during charge, which is close to the theoretical capacity of 128 mAh $g^{-1}$. Until moderate C-rates of C/5, the for KTP/C typical distinct voltage plateau around 1.5–1.7 V (discharge) and 1.8–2.0 V (charge) is visible, which indicates a two-phase reaction between the redox-couple $KTi_2(PO_4)_3$ and $K_3Ti_2(PO_4)_3$ for the KTP/C composites. The two-phase behavior was further confirmed by additional operando XRD analysis as the main hkl reflexes 113 and 116 gradually vanish and new reflexes at lower Bragg angels appear during cycling (Figure S3a). The polarization in the coin-cell-type half-cell setup increased during oxidation by 100 mV from C/20 to C/10 (and another 100 mV to C/5). The voltage hysteresis of around 500 mV at C/10 is in good agreement with other carbon-coating approaches reported in literature [19–21]. The refined particle architecture combines nanocrystalline primary particles, unique granule microstructure (open porosity ≈49%), carbon coating (4.2%), and a high specific surface area (≈49 $m^2 g^{-1}$), enabling short diffusion lengths inside the KTP/C active material and percolating electronic network inside the granules and may also promote improved charge-transfer kinetics [19, 21, 30, 33, 38]. At higher C-rates of C/2 and 1C, an increasing polarization is apparent, which is probably attributed to two different effects: an increased polarization of the metallic potassium anode [9, 12–15] and solid-state diffusion limitations of K-ions in the bulk active material phase [27, 39–41].

*2.2.1.2 | KTP/C as RRE (KTP-RE).* A prerequisite for REs is small potential drifts, ideally on a mid- to long-term scale. Therefore, active materials with a distinct and flat redox plateau over a wide state of charge interval are interesting candidates as potential RE when partly charged. In a first experiment, the KTP/C was thus discharged versus K-CE at C/20 to the voltage plateau at around 1.6 V versus $K^+/K$, and the open circuit voltage (OCV) was recorded for over 300 h (Figure 4b). After an initial relaxation of around 48 h, the KTP/C potential drift slows down and approaches a stable value at about 1.84 V over the course of the following ~250 h in a coin-cell-type half-cell setup, which corresponds to a drift rate of 4.1 mV $d^{-1}$ (i.e., 0.17 mV $h^{-1}$) in the interval from $t = 75$ to $t = 325$ h. This is in the same range as a previously presented RE based on Bi–$Bi_2K$ alloy: ~0.1 mV $h^{-1}$) [7]. Table 2 summarizes RE characteristics of previously reported systems. Based on previous works [8, 9], a significant fraction of this drift is likely associated with a drift of the potassium potential rather than the KTP/C.

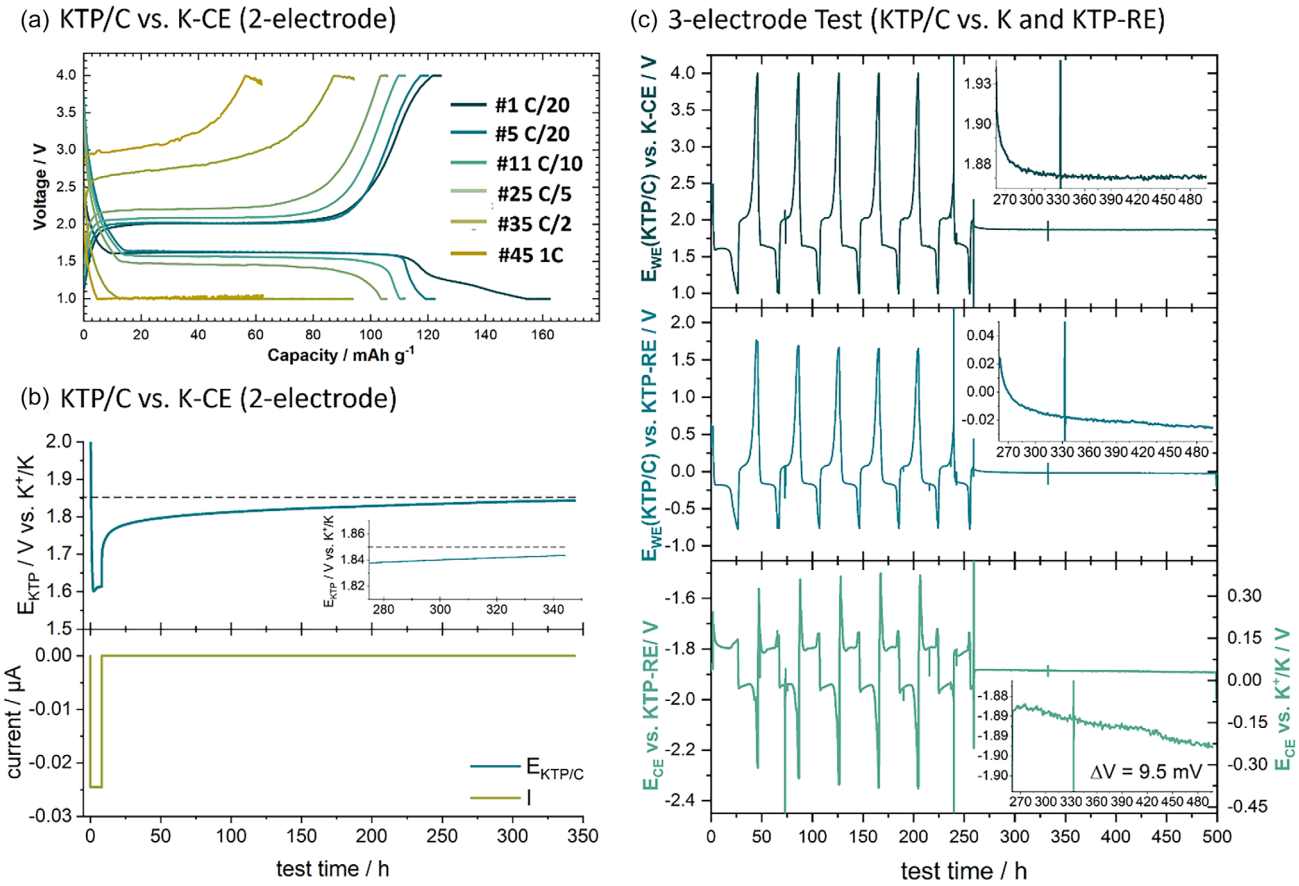


**FIGURE 4** | Electrochemical characterization of KTP/C composites in a half-cell setup against a potassium metal counter electrode: (a) C-rate capability test for KTP/C-700 from C/20 to (1C =128 mA $g^{-1}$), (b) self-discharge test of KTP/C-650 with discharge to the voltage plateau around 1.6 V versus $K^+$/K and subsequent measurement of the OCV (coin cell setup), and (c) three-electrode measurement with a KTP/C-700 RE, a KTP/C-700 WE and a potassium metal CE. Cycling was performed at C/20 in a voltage window of 1.0–4.0 V (WE vs. CE). The insets show the potential drifts over an extended time period of over 200 h at OCV.

In a three-electrode cell, KTP/C was further evaluated as RE using a modified setup previously reported by Bünzli et al. [45] and Panasenko et al. [9] (Figure S10). The RE pin was loaded with a KTP/C electrode composite (comprising KTP/C:SuperC65:PVDF in a 8:1:1 mass ratio, labeled as KTP-RE in the following). First, the RE-pin was conditioned, following the procedure described above (voltage transient provided in Figure S4). The three-electrode cell consisted of a KTP/C WE, potassium metal CE, and a KTP-RE and was cycled over 6.5 cycles before the electrode was put on a targeted OCV potential of 1.8 V for a self-discharge test. Figure 4c (left panel) shows the potential profiles of KTP/C WE versus $K^+$/K (top panel), KTP/C WE versus KTP-RE (middle panel), and K-CE versus KTP-RE (bottom panel). The potential drift experiment is shown in the enlarged right panel of Figure 4c.

For the KTP/C WE in this three-electrode setup, the same specific charge capacity (123 mAh $g^{-1}$) and the potential profiles (Figure S5a) are in good agreement with the two-electrode half-cell results shown in Figure 4a as well as with previous KTP-related studies [19, 20, 38, 46]. The experiment also illustrates that the voltage hysteresis between charge and discharge of KTP/C WE is only around 200 mV at C/20 with respect to the KTP-RE, instead of about 400 mV for the respective coin-cell-type half-cell against K-CE (Figure 4a). This is further evidence that a substantial contribution to the cell polarization originates from the potassium metal (polarization was calculated as the potential difference at the center of the voltage plateau of KTP/C). Similarly, the three-electrode cell setup allows one to accurately track the potential transient of the K-CE electrode, showing the characteristic plating-stripping features of an alkali metal electrode that are usually superimposed on the WE voltage transient in conventional two-electrode tests [47, 48]. Starting from stripping steps, the K-CE potential first decreases and then plateaus around the midpoint of the sequence (at around −1.8 V vs. KTP/C RE). At the end, a peaking behavior is seen, which usually indicates stripping of bulk K-metal. In the plating steps, typical nucleation and growth behavior with decreasing overpotentials are seen. In the section of the sequence, the potential spikes (both for KTP/C WE and K-CE) are likely due to a blocking boundary effect as a result of the high upper cut-off of 4.0 V (capacitive effect when KTP/C insertion reaction stops). During the open-circuit sequence, after 6.5 cycles, the KTP/C WE and the K-CE show a minor drift of less than 10 mV over 200 h (Figure 4c, right panel) versus KTP-RE, accounting for a drift rate of only 0.05 mV $h^{-1}$ and thus even lower than other reported REs in the PIB field [7–9]. Other benefits of the KTP-RE include that the active material operates within the electrolyte stability window of commonly used organic electrolytes [49] as well as the repeatable use of the KTP-RE pin after a rinsing (with the

**TABLE 2** | Comparison of reference electrode systems suggested for PIB applications and related cell chemistries. Cell setups and measurements on the reference potential and drift rate may vary.

| Reference electrode | Electrolyte | Avg. potential (vs. $K^+/K$), V | Drift rate,[a] mV h−1 | Ref.[b,c] |
|---|---|---|---|---|
| Potassium-related literature | | | | |
| Bi–$BiK_2$ alloy | 2 M KFSI in TEP (30 °C) | 1.07 ± 0.003 V | −0.1 ± 0.1 (over 80 h) | Jagger et al. [7] |
| Ag\|AgCl | 0.75 $KPF_6$ in EC:DEC | 2.55 V (−3.59 V vs. $Fc^+/Fc$) | <0.01 (over 100 days) | Panasenko et al. [9] |
| KTP/C | 0.5 M $KPF_6$ in EC:PC | 1.84 V | 0.17 (over 250 h) | This work |
| Related cell chemistries | | | | |
| $Ag\|AgNO_3$ | 1 M $NaClO_4$ in PC | −0.285 V vs. $Ag^+/Ag$ | 0.21 (over 45 h) | Lee and Tang [42] |
| Sodiated tin-wire micro-RE | 1 M $NaPF_6$ in EC:DMC | –0.11 V vs. $Na^+/Na$ | <0.01 (over 100 h) | Linsenmann et al. [43] |
| Activated carbon | 1 M $LiPF_6$ in EC:DMC | 3.07 vs. $Li^+/Li$ (−3.25 V vs. $Fc^+/Fc$) | 0.142 (over 100 h) | Ruch et al. [44] |

[a]Drift rates were determined after OCV relaxation interval (material-dependent; different in each study).
[b]Tested in absence of K-metal (Pt-WE, Cu-CE; electrolyte: 10 mM $Fc^+/Fc$, 100 mM $KPF_6$ in EC:DEC.
[c]Tested in glassy carbon/Ag-RE/Na-CE 3-e setup (Ag-RE and Na-CE in separate cell compartments).

electrolyte solvent) and drying (overnight) step. In case of minor potential drifts, the RE could be reconditioned by polarization against K-metal prior to reuse in three-electrode measurements. All of the discussed results underline the great potential of the KTP/C as RE for PIBs, while to our knowledge, an insertion-type material is used for the first time as a RE for PIBs. It simplifies and allows a more precise characterization of active materials and electrolyte properties, even at higher C-rates, as the overpotentials of the potassium metal CE could be bypassed by controlling the WE versus KTP-RE potential.

### *2.2.2 | Electrochemical Characterization of KTPO/C Composites*

This section investigates the electrochemical properties of KTPO/C composites, leveraging the three-electrode setup with KTP-RE established in the previous section.

The voltage profile of the rate capability test is shown in Figure 5a. At C/20, the maximum charge capacity of KTPO/C reaches the theoretical capacity of 135 mAh $g^{-1}$ in the fifth cycle. Similar to the KTP/C composites, KTPO/C shows lower voltage hysteresis of <250 mV between the prominent voltage plateau at around 1.15 V versus $K^+/K$ at C/20, comparable to previous studies [19–21, 25, 26]. Operando XRD experiment (Figure S3b) suggests a two-phase composition over a wide potential range between 0.3 and 1.15 V. The initial 40 mAh $g^{-1}$ on the first cycle displays a slower capacity decay to the 1.15 V plateau, which is likely a contribution of the titanium oxide impurity phase (Figure 3c) [50]. A weak reflection of the impurity phase near 12.5°, further indicates minor redox activity of the impurity phase upon cycling. With increasing C-rate, the polarization increases considerably, which is also reflected in lower charge capacities. At C/10, still 118 mAh $g^{-1}$ are retained, while the polarization on the voltage plateau increases by almost 100 mV from C/20 to C/10. A notable capacity drop is observed at C/5 to 80 mAh $g^{-1}$ upon charge. At C/2, less than 30 mAh $g^{-1}$ was retained. Most of the measured capacity arises from the constant voltage step that is not rate-dependent. Interestingly, the voltage hysteresis and capacities recover after the rate test at a constant C-rate of C/5 from cycle 51 onward, reaching 118 mAh $g^{-1}$ in the 95$^{th}$ cycle. (Figure S6) This could be an indication that most of the polarization is caused by the K-CE as the electrochemically active surface area increases significantly during cycle-aging due to mossy/dendritic deposits, thus reducing the resistance of this cell component [9, 12–16]. The high cycling stability combined with high charge capacity at a low C-rate of C/20 and C/10 could be linked to the unique microstructure of the hierarchically structured KTPO/C composites, enabled by the carbon coating (5.2%) in combination with high specific surface (27.7 $m^2$ $g^{-1}$) and open porosity (39%) [25, 26, 30, 33, 36].

The self-discharge test in Figure 5b (similar to KTP/C) showed that the potential of the KTPO/C composite was stable for around 48 h and commences to drift strongly afterward, thus rendering KTPO/C unsuitable as a RE. However, its flat voltage plateau around 1.15 V can be of use as an alternative negative electrode (see below).

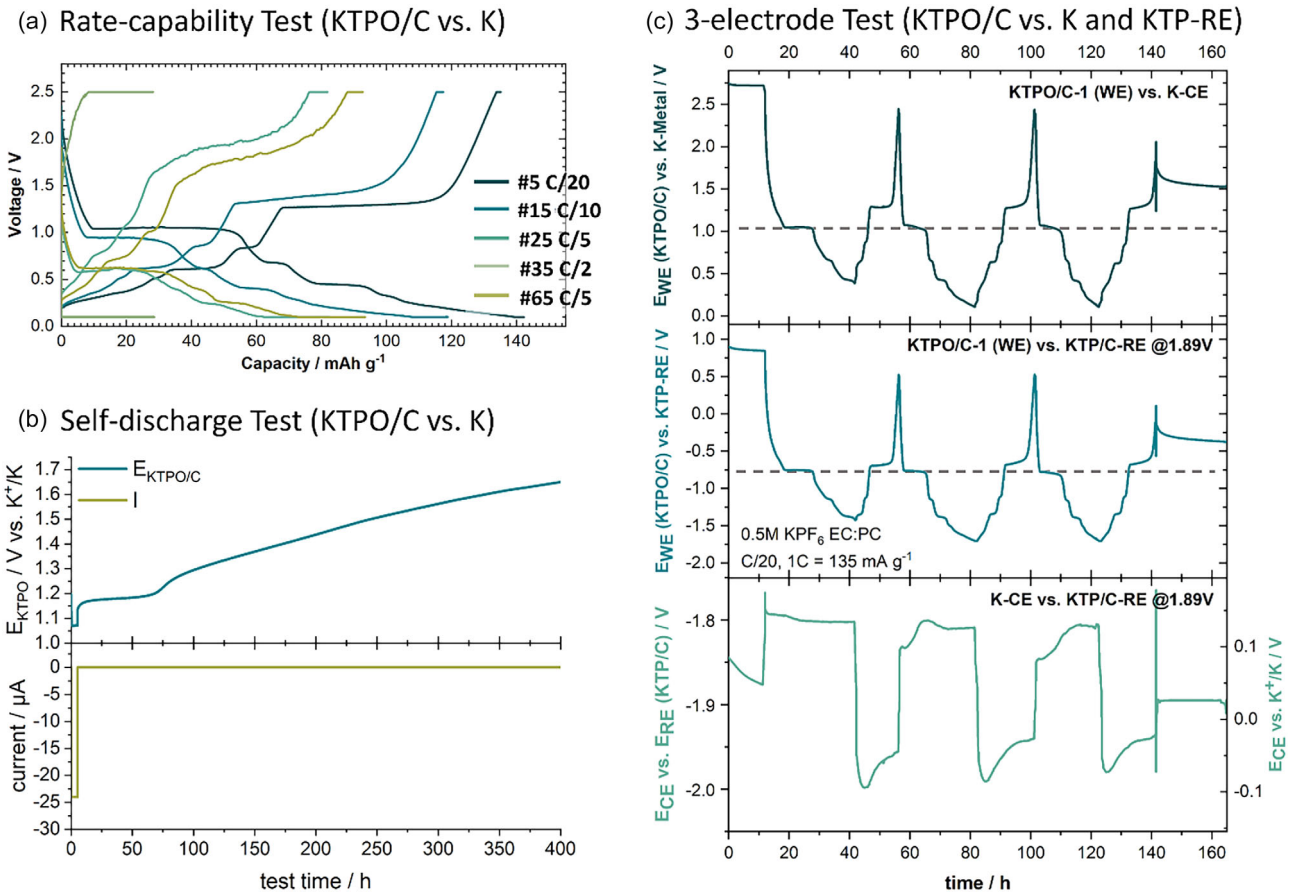


**FIGURE 5** | Electrochemical characterization of KTPO/C composites in a half-cell setup against a potassium metal counter electrode: (a) C-rate capability test for KTPO/C from C/20 to C/2 (and cycling at constant C/5 after cycle 50; 1C = 135 mA $g^{-1}$), (b) self-discharge test of KTPO/C with discharge to the voltage plateau around 1.07 V versus $K^+/K$ and subsequent measurement of the OCV, (c) three-electrode measurement with a KTP/C-700 RE, a KTPO/C WE and a potassium metal CE. Cycling was performed at C/20 in a voltage window of 0.1–2.5 V (WE vs. CE).

To further study the electrochemical properties of KTPO/C, three-electrode-experiments with a KTPO/C WE, K-CE, and KTP-RE were carried out (Figure 5c). In a direct comparison, both voltage profiles and capacities of the KTPO/C composite electrodes coincide in shape and length (Figure S7), and the voltage hysteresis in the three-electrode cell was about 100 mV smaller than in the two-electrode cell. The voltage transient of K-CE (vs. KTP/C RE) shows that during reduction (plating on K-metal), a significant overpotential of more than 100 mV is built-up (dendrite nucleation and growth), even at C/20. The experiment aims to demonstrate that the voltage hysteresis of KTPO/C accounts for less than 70 mV at C/20 when measured against KTP-RE, whereas in a two-electrode half cells (against K-CE), the hysteresis amounts to a total of up to 200 mV. This underlines the issue of using potassium metal in even basic electrochemical testing routines, as a limiting factor for cycle life, cell resistance, and rate limitation.

### *2.2.3 | Assessment of KVP/C With KTPO/C as Diagnostic Anode*

The voltage profile of KTPO/C shows a flat redox plateau at around 1.15 V for ca. 50 mAh $g^{-1}$, as seen in Figure 5a. When the electrode only operates within the capacity interval of this 1.15 V plateau, it can serve both as a CE and (internal) pseudo-RE. In addition, the redox potential is within the electrochemical stability window of most common liquid electrolyte components, except for additives such as FEC [49]. In a full-cell configuration against a cathode material, the length of the plateau is then only limited by the areal capacity of the KTPO/C electrode. In other words, for high N/P ratios, the KTPO electrode potential can be maintained at the 1.15 V over the entire cycling sequence. This approach is similar to earlier works by Dose et al. [23, 24] on the changes in lithium inventory in $LiFePO_4$/Si cells. The authors referred to the oversized $LiFePO_4$ electrode as a diagnostic cathode.

Herein, we expand this approach for the first time to a PIB system, using KTPO/C as a diagnostic anode and a carbon-coated microstructured $K_3V_2(PO_4)_3$ (KVP/C) positive electrode. The KVP/C cathode was prepared by a similar synthetic approach, as reported previously by our group [30]. The practical capacity of KVP/C matches well with the length of the redox plateau of KTPO/C (around 55 mAh $g^{-1}$ in three-electrode half-cell against KTP-RE, Figure S7). For three-electrode measurements, the KTP/C RE was used.

The data in Figure 6a highlight that the KTPO/C potential remains constant over the entire cycling range when the accessible voltage and capacity range are limited to the first voltage

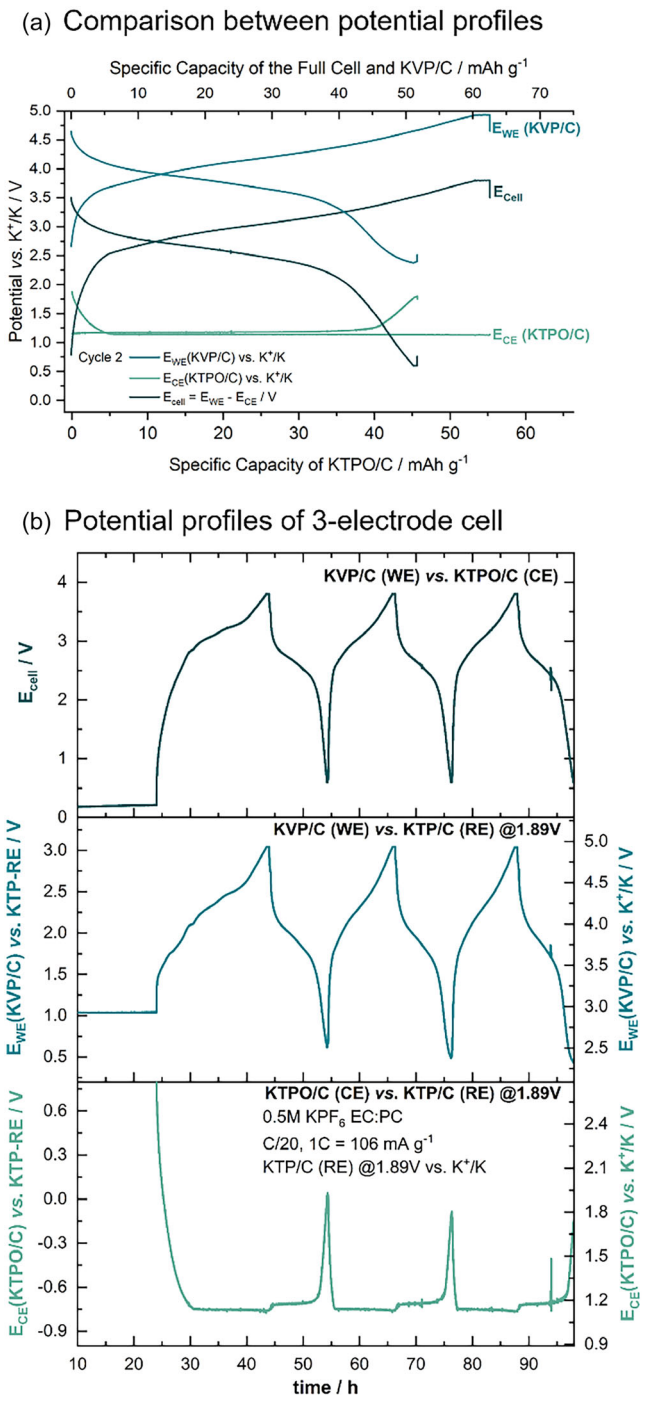


**FIGURE 6** | Three-electrode-cell measurement with KVP/C as WE, an KTPO/C CE (unconditioned) and the KTP-RE with (a) the cell's potential profiles against specific charge for the cell voltage ($E_{cell}$), the working electrode potential $E_{WE}$(KVP/C) and counter electrode potential $E_{CE}$(KTPO/C) (vs. KTP-RE) on cycle #2 and (b) the same potential profiles against time over the first three cycles. Galvanostatic cycling was performed at C/20 (1C = 106 mA $g^{-1}$), in a 0.5 M $KPF_6$ EC:PC (1:1) electrolyte formulation.

plateau, except for 5 mAh $g^1$ at the start (charge) and end (discharge), respectively. This could be further tuned by changing the N/P ratio. Accordingly, the voltage profile of the cell voltage, $E_{cell}$, and the KVP/C potential are identical, but shifted by the KTPO/C potential. This indicates already the good suitability of the KTPO/C composites as a diagnostic anode for evaluation of cathodic materials.

For the demonstration of the last experiment, the use of KTPO as DE in a two-electrode setup, preconditioning of the KTPO/C CE was performed prior to the full cell experiments (Figure S9) to eliminate some of the irreversible first cycle losses and to slow down the depletion of the potassium inventory.

The KTPO/C//KVP/C full cell in a coin-cell setup was tested over 60 cycles at different current densities in the voltage window of 0.8–3.7 V, as shown in Figure 7a(top). The results were compared to a corresponding half-cell configuration with K-CE in a coin-cell-type half-cell in Figure 7b(top). A three-electrode data (KVP vs. precycled KTPO, with KTP-RE) are provided for comparison in Figure S11 (using the cell setup shown in Figure S10). The KVP/C composites display higher specific discharge capacities than the half-cell, yielding an additional 10–20 mAh $g^{-1}$ over the first 20 cycles at cycling rates of C/20 and C/10. The lower discharge capacity in the 1$^{st}$ cycle is caused by a step time limit during cycling; thus, the upper voltage cut-off of the cell was not reached. The capacity increase is likely due to (1) shifts in the upper voltage cut-off of KVP/C and (2) considerably reduced reactivity of the KTPO/C anode compared to negative electrodes operating at potential close to 0 V versus $K^+$/K. Based on the three-electrode data, an upper cut-off limit of 3.7 V versus KTP-RE corresponds to nearly 4.8 V versus $K^+$/K. In contrast, in our previous work, the upper cut-off limit for KVP/C (vs. $K^+$/K) was 4.5 V. Other studies limited the upper cut-off to 4.6 V versus $K^+$/K [51–53]. The respective section of the voltage profiles increases nearly after the plateau at 3.2 V versus KTP-RE, adding around 20 mAh $g^{-1}$ (illustrated best for the 5$^{th}$ cycle). The same plateau corresponds to a potential of 4.4 V versus $K^+$/K in the half cell. The last cycling stage between plateau and cut-off only adds around 10 mAh $g^{-1}$. Taking into account the potential shift due to the KTPO/C quasi-reference (about 1.15 V at C/20), then an additional 100 mV in overpotential originates from the use of a K-CE.

The cycling data of the KTPO/C//KVP/C full cell in Figure 7, bottom row, suggests a minor capacity fade over the first test interval at C/20 and C/10, whereas the KVP/C half-cell displays constant capacities with small capacity steps when the rate increases from C/20 to C/10 and then to C/5. At C/5, both cells show similar capacities of 58 mAh $g^{-1}$ and display a similar capacity drop when the rate is increased to C/2 and 1C (the higher upper cut-off might buffer a stronger drop for the full cell). Interestingly, when the current density is set back to C/5 in the last cycling interval, the capacity recovers fully in the case of the KTPO/C//KVP/C full cell, while the half-cell configuration suffered from a small loss in this step.

In summary, we established hierarchically structured titanium-phosphate-based active materials for their application in (insertion-type) reference and DEs. Three-electrode cells equipped with these novel electrodes present a means to bypass polarization and crosstalk biases that originate from metallic potassium electrodes during the study of electrode materials in half-cell configurations [16]. The newly developed full-cell setup with a precycled KTPO/C as diagnostic anode was presented as a potential enabler for more accurate and precise electrochemical

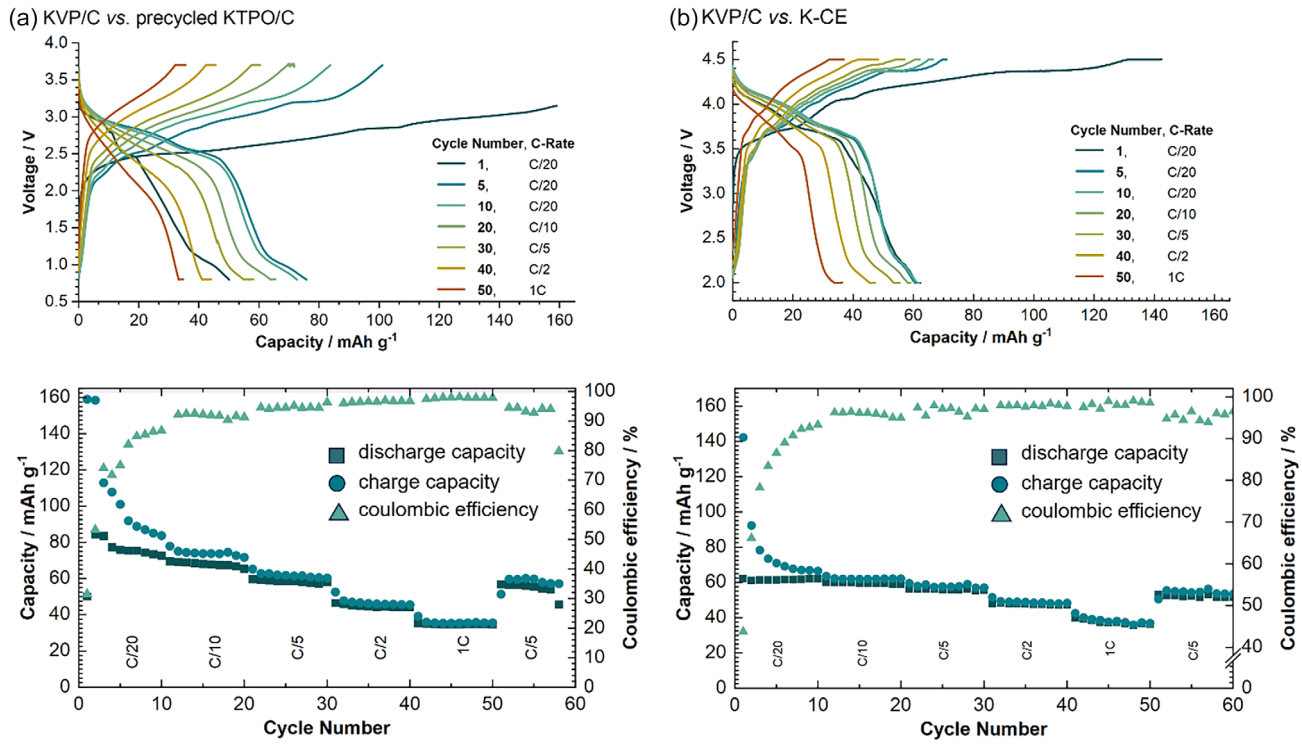


**FIGURE 7** | Electrochemical characterization of a full-cell setup with a KVP/C WE and a precycled KTPO/C DE (a) compared to the half-cell performance of a KVP/C WE against a potassium metal CE (b) at different rates. The voltage profiles are shown in the top row for selected cycles. In the bottom row shows the specific charge and discharge capacities and corresponding Coulombic efficiencies. C-rates were always calculated based on the theoretical capacity of KVP/C (1C = 106 mAh $g^{-1}$). Determined capacities are always related to the composite active material masses of the KVP/C WE.

characterization of active materials for PIBs. For easier integration of the DE (e.g., to remove the conditioning step), further investigations are needed to assess the structure–property relationships between particle microstructure and morphology and electrochemical characteristics. This approach may extend to alternative Ti-based phosphates as well as electrode coating properties (including densification). Overall, the DE approach will be of interest where isolated electrode-electrolyte interactions ought to be investigated and interferences from CEs ought to be avoided. Therefore, we see a particular potential in the area of advanced electrolyte development to reduce crosstalk and self-discharge processes.

## 3 | Conclusion

In this work, two Ti-based polyanionic materials, KTP/C and KTPO/C, were successfully implemented as an RE or DE for an improved electrochemical characterization of active materials for PIBs. The synthesis of hierarchically structured KTP/C and KTPO/C composites allowed their application as an RE or DE for PIBs. The potential of the KTP/C composites stabilizes after 48 h and is stable on a long-term scale (>250 h), enabling its implementation as an insertion-type RE for the first time for PIBs. Instead, the potential of the KTPO/C composite stabilizes quickly, but drifts strongly after 48 h, which make this material unsuitable as a RE for PIBs. Nevertheless, the kinetic limitation of potassiation/depotassiation is low for the KTPO/C composites, which allows it used a stable DE in a full-cell configuration. A comparison of the electrochemical performance of KVP/C in a full-cell and half-cell configuration, showed a significantly underestimated performance of the KVP/C in a half-cell setup. With the developed KTPO/C as a DE and KTP/C as a RE for PIBs, this study paves the way to bypass the dramatic negative impact of metallic potassium on and allow a more precise and reliable electrochemical characterization of active materials for PIBs.

## 4 | Materials and Methods

### 4.1 | Synthesis of Hierarchically Structured Titanium Phosphates

#### *4.1.1* | *Potassium Titanium Phosphate ($KTi_2(PO_4)_3$, KTP)*

For the synthesis of KTP/C, as reactants $K_2CO_3$ (VWR, Germany), $TiO_2$ (DEGUSSA/Evonik, Germany), and $NH_4H_2PO_4$ (VWR, Germany), as well as β-lactose (Sigma-Aldrich, USA) as carbon source, were used. The reactants $K_2CO_3$, $TiO_2$, and $NH_4H_2PO_4$ were thoroughly mixed in the stochiometric ratios of 1:4:6, while 10 wt% excess of $K_2CO_3$ was used. Mixing was achieved by planetary ball-milling in 2-propanol for 8 h (1 h milling and 1 h break alternating) at 250 rpm. Ratio of reactants:milling balls:2-propanol was set to about 1:4:3.5, while 3002 g of $ZrO_2$ ball with a diameter of 3 mm were used for milling. After ball-milling, 2-propanol was evaporated and the mixture of reactants was dried overnight at 80 °C.

The calcination of the pure KTP was performed under synthetic air (80% $O_2$/20% $N_2$) in a retort oven. The heating rate was set to 1 K/min until 400 °C, where the temperature was held for 2 h. Afterward, the heating rate was increased to 3 K/min until 850 °C for the calcination of 5 h at this temperature. The samples were naturally cooled down to room temperature afterward. Subsequently, the phase pure KTP samples were prepared for the spray-drying process to create hierarchical microstructures. Therefore, 12.5 wt% of β-lactose was added to the pure KTP, and the samples were ball-milled in a planetary ball-mill with deionized water as dispersion media. Milling time was 12 h in total (2 × 6 h milling and 3 h break in between) at 250 rpm, while 300 g of deionized water and 300 g of $ZrO_2$-balls with a diameter of 3 mm were used for 50 g of the powder mixture. For the following spray-drying process, the solid content was adjusted to 8–10 wt% and 1 wt% of poly(ethylene glycol) (PEG) and PAA, as dispersing agent and binder additive, were added. The inlet temperature was 210 °C, the outlet temperature 112 °C, as a process gas, nitrogen was used. The samples were spray-dried at 30.000–35.000 rpm of the atomizer wheel. The tower and cyclone fraction were combined and then subjected to a further heat treatment in a retort oven under inert Ar atmosphere. The heating rate was set to 5 K/min, while the end temperature was varied between 650 and 850 °C in steps of 50 °C. Holding time at the end temperature was 5 h. Afterward, the samples were cooled down naturally to room temperature, sieved, and stored under ambient conditions.

#### *4.1.2 | Potassium Titanyl Phosphate ($KTiOPO_4$, KTPO)*

For the synthesis of KTPO/C, as reactants $K_2CO_3$ (VWR, Germany), $TiO_2$ (DEGUSSA/Evonik, Germany), and $NH_4H_2PO_4$ (VWR, Germany), as well as sucrose (Sigma-Aldrich, USA) and β-lactose (Sigma-Aldrich, USA) as carbon sources, were used. The reactants $K_2CO_3$, $TiO_2$, and $NH_4H_2PO_4$ together with 7.5 wt% sucrose were thoroughly mixed in the stochiometric ratios of 1:2:2. Mixing was achieved by planetary ball-milling in 2-propanol for 8 h (1 h milling and 1 h break alternating) at 250 rpm. Ratio of reactants:milling balls:2-propanol was set to about 1:3:2.5, while 300 g of $ZrO_2$-balls with a diameter of 3 mm were used for milling. Afterward, 2-propanol was evaporated and the mixture of reactants was dried overnight at 80 °C.

The calcination of the KTPO/C composite was performed under an inert Ar atmosphere in a retort oven. The heating rate was set to 1 K/min until 450 °C, where the temperature was held for 2 h. Afterward, the heating rate was increased to 3 K/min until 850 °C for the calcination of 12 h at this temperature. The samples were naturally cooled down to room temperature afterward, and the KTPO/C composite material was obtained as a fine black powder. Subsequently, the KTPO/C composite was prepared for the spray-drying process to create hierarchical microstructures. Therefore, 15 wt% of β-lactose was added to the KTPO/C composite and the samples were ball-milled in a planetary ball-mill with deionized water as dispersion media. Milling time was 12 h in total (2 × 6 h milling and 3 h break in between) at 250 rpm, while 300 g deionized water and 300 g of $ZrO_2$ balls with a diameter of 3 mm were used for 50 g of the powder mixture. For the following spray-drying process, the solid content was adjusted to 8–10 and 0.5 wt% of PEG and PAA, as dispersing agent and binder additive, were added. The inlet temperature was 210 °C, the outlet temperature 112 °C, as a process gas, nitrogen was used. The KTPO/C composite was spray-dried at 30.000–35.000 rpm of the atomizer wheel. The tower and cyclone fraction were combined and then subjected to a further heat treatment in a retort oven under an inert Ar atmosphere. The heating rate was 5 K/min until 850 °C, where the temperature was held for 5 h. Afterward, the samples were cooled down naturally to room temperature, sieved, and stored under ambient conditions.

#### *4.1.3 | Potassium Vanadium Phosphate ($K_3V_2(PO_4)_3$/C, KVP/C)*

The synthesis of hierarchically microstructured KVP/C composites as cathode-active material was previously reported in reference [30].

### 4.2 | Material Characterization

#### *4.2.1 | Thermal Analysis TG/DSC-IR*

Thermal analysis was performed with a TGA STA449 (Netzsch, Germany) directly coupled with a FT-IR Vertex 70 (Bruker, Germany) to analyze gaseous reaction products. The heating rate was 5 K/min up to 1000 °C under Ar (KTPO/C) or synthetic air (KTP/C)-atmosphere, respectively. The transfer line and FT-IR gas measurement cell were heated to 200 °C in advance. IR traces of the gaseous byproducts were calculated by subtracting a baseline in the respective IR-spectra to further eliminate measuring artifacts from the FT-IR gas measurement cell.

#### *4.2.2 | XRD*

Powder XRD measurements were recorded at a D2 diffractometer (Bruker, Germany) using Cu-Kα-rays between 10°–60°. Rietveld refinements were performed using the software TOPAS (Bruker, Germany). Crystallite size was estimated by a double-Voigt approach as implemented in the TOPAS software.

#### *4.2.3 | SEM*

Electron micrographs were recorded using a field-emission scanning electron microscope (Supra55, Carl Zeiss GmbH, Oberkochen, Germany) at different acceleration voltages and magnifications. Cross-sections of the electrodes were obtained via ion-beam milling using an EM TIC3X system (Leica Microsystems GmbH, Wetzlar, Germany), employing argon ions at an accelerating voltage of 6 kV and a gun current of 2.2 mA.

#### *4.2.4 | Porosimetry*

To evaluate the specific surface of the particles, $N_2$-sorption measurements at Gemini VII 2390a (Micromeritics, USA) were performed. Brunauer-Emmett-Teller (BET) evaluation was used in the linear region of the adsorption isotherm with a positive C-value. Prior to characterization, all samples were predried overnight at 120 °C under vacuum.

Mercury porosimetry was used to evaluate the internal porosity of the particles with a CEI PASCAL 1.05 (Thermo Electron, USA). The internal porosity $P$ was calculated by use of the internal specific pore volume $V_P$ below a defined threshold value

based on the following formula: $P = \frac{V_p}{V_p + \frac{1}{\rho}}$ with the density of the different composites $\rho$. The threshold was used to distinguish between intergranular and intragranular porosity. For KTPO/C, a density $\rho$ of 3.03 g cm$^{-3}$ (Norberg et al. [34], ICSD-182657, ICSD release 2025.1) and for KTP/C, a density $\rho$ of 2.99 g cm$^{-3}$ (Lunezheva et al. [31], ICSD-67091, ICSD release 2025.1) was used for the calculation of the internal specific pore volume.

#### 4.2.5 | *Particle Size Distribution*

Static light scattering was applied to measure the particle size distributions using a Horiba LA50 (Retsch Technology, Germany). Internal sonification was used to destroy any possible agglomerates. Measurements were performed five times per sample and mean values for the volume-weighted particle size distribution were calculated.

#### 4.2.6 | *ICP-OES*

Chemical composition was evaluated by use of ICP-OES with iCAP7600 duo (Thermo Scientific, USA). The composites were dissolved in nitric acid and/or hydrochloric acid prior to measurement. The elemental composition was measured three times for each sample and mean values were calculated. The carbon content was analyzed with a CS analyzer (inductar CS cube, Elementar Analysensysteme GmbH, Germany).

### 4.3 | Cell Assembly and Electrochemical Characterization

#### 4.3.1 | *Electrode Preparation*

The active material powders were first dried at 120 °C under vacuum in a vacuum oven (Buechi, Switzerland) and sieved with a 32 µm sieve. Subsequently, the KTP/C or KTPO/C samples were mixed in a Speedmixer with a premixed slurry containing PVDF (Solef PVDF 5130/1001, Solvay), C65 (C-Nergy Super C65, TIMCAL), and NMP in a ratio of KVP/C:C65:PVDF of 80:10:10. The well-mixed and homogeneous slurry was then cast onto Al foil with a wet-film thickness of 200 µm by a doctor blade. The electrode sheets were cut into 12 mm (half-cell), 14 mm (anodes/DEs for full cells), and 16 mm disks with a 8 mm hole in the center (three-electrode setup, WE). The electrodes were then dried at 120 °C under vacuum in a Büchi oven and transferred without further exposure to ambient air into an Ar-filled glovebox. Typical mass loadings for the electrode active material were between 3.5 and 4.5 mg/cm$^2$.

#### 4.3.2 | *Cell Assembly*

All cells, either in a coin-cell CR2032 or three-electrode setup, were assembled in Ar-filled gloveboxes ($H_2O$ and $O_2 <$ 0.1 ppm). The theoretical capacity of KTP/C was defined as 128 mAh/g and that of KTPO/C as 135 mAh/g. For KVP/C ($K_3V_2(PO_4)_3$) positive electrodes in full-cell experiments, the theoretical capacity of KVP/C was defined as 106 mAh/g (the practical capacity was around 60 mAh/g) [30].

#### 4.3.3 | *Half-Cell Tests (Coin Cells)*

For coin-cell type half cells as WE, the different KTP/C or KTPO/C samples were used as 12 mm disk electrodes, while potassium metal (chunks in mineral oil, 98%, Thermo Scientific Chemicals) was used as anode. The potassium metal was cut into small pieces, washed thoroughly and stored over n-hexane inside the glovebox. For preparation of potassium metal anodes, the potassium metal was rolled and squeezed into thin sheets inside a nitrile glove. After that, 14 mm disk electrodes were punched out of the thin potassium metal sheets to use them as the anode.

As an electrolyte, a solution of 0.5M $KPF_6$ in EC:PC (1:1 by volume) was used, while the volume was set to 150 µL. As a separator, Whatman GF/C-separators with a diameter of 16 mm were used for the coin-cell format half cells. Galvanostatic charging (CCCV) with a CV step was performed at a Biologic BCS (Biologic, France) in a voltage range from 1.0 to 4.0 V (KTP/C) and 0.1–2.5 V (KTPO/C in a half-cell configuration. GCPL measurements were performed at the following C-rates: C/20, C/10, C/5, C/2, and 1C. For KTP/C and KTPO/C, in all half-cell configuration, cycling always starts with discharge, as they are evaluated as anodic materials.

#### 4.3.4 | *Self-Discharge Tests*

The potential drift under OCV was measured in half-cell configurations using either KTP/C or KTPO/C WEs versus potassium metal. The composites were discharged (at C/20) to the voltage plateau around 1.6–1.7 V for KTP/C and around 1.0 V for KTPO/C and kept under open-circuit conditions without any applied current after the plateau was reached for several days.

#### 4.3.5 | *KVP//KTPO Two-Electrode Full Cell Tests*

For all full cell setups in a CR2032-type coin-cell, 14 mm disk electrodes of KTPO/C as DEs were preconditioned in a half-cell setup against potassium metal. For preconditioning, the KTPO/C DE were cycled at C/30 in a voltage range of 0.9–1.5 V versus potassium metal for two cycles to reduce irreversible losses in the subsequent full cell setup and stopped at the voltage plateau of KTPO/C.

For CR2032-type full cells, the preconditioned KTPO/C electrodes were used as a DE against a 12 mm KVP/C electrode. The wet film thickness of the KVP/C WE for the full cell setups was reduced to 100 µm to bypass a possible capacity limitation of the full cell caused by the KTPO/C DE (the N/P ratio was around 1:1, assuming practical capacities of 60 mAh g$^{-1}$ for KVP/C and 50 mAh g$^{-1}$ for KTPO/C). As an electrolyte, a solution of 0.5 M $KPF_6$ in EC:PC (1:1 by volume) was used, while the volume was set to 150 µL. As a separator, Whatman GF/C-separators with a diameter of 16 mm were used for the coin-cell format half cells. Galvanostatic charging (CCCV) with a CV step was performed at a Biologic BCS (Biologic, France) in a voltage range from 0.8 to 3.7 V. GCPL measurements were performed at the following C-rates: C/20, C/10, C/5, C/2, and 1C. All stated capacities refer to the composite mass of the KVP/C WEs and not the active material content.

#### 4.3.6 | *Experiments in Three-Electrode Cells*

Cell setups and RE conditioning and cycling protocols in a coin-cell-type cell setup were established in our previous work by Panasenko et al. [9]. The experimental setup is schematically shown in Figure S10.

#### 4.3.7 | *RE (KTP-RE) Preparation*

To utilize KTP/C as a RE, a conductive metal pin was coated with an electrode slurry with KTP/C as active material, mixed as described above. This pin was preconditioned in a classical half-cell configuration against a 14 mm potassium metal disk electrode. Cycling was performed with a current of 1 µA until the voltage plateau of KTP/C around 1.6–1.7 V was reached. Subsequently, the current was stopped at the voltage plateau around 1.6–1.7 V, and the pin was kept at open-circuit condition for at least several days for relaxation of the KTP/C into equilibrium state. Afterward, the KTP/C-coated pin could be utilized as RE in potassium-ion-battery half- and full-cell configuration.

#### 4.3.8 | *Three-Electrode Half-Cell Configurations*

The cell setup comprised a KTP/C or KTPO/C ring electrode (16 mm in diameter with 8 mm hole in its center) as WE, a 14 mm potassium metal disk as CE, and a KTP-RE pin (Figure S10). As a separator, an 18 mm Whatman GF/C was used, while the electrolyte volume of 0.5 M $KPF_6$ in EC:PC (1:1 by volume) was increased to 300 µL. Galvanostatic charging (CCCV) with a CV step was performed at a Biologic SP-200 (Biologic, France) in a voltage range from 1.0 to 4.0 V KTP/C or 0.1–2.5 V (KTPO/C) at C/20. The cell voltage (WE vs. CE), WE potential (WE vs. RE), and CE potential (CE vs. RE) were recorded simultaneously over time. Additionally, for KTP/C as WE, the OCV was recorded for several days after cycling at C/20.

#### 4.3.9 | *Three-Electrode Full-Cell Configurations*

Full cell configurations contained a KVP/C ring electrode as WE (outer diameter: 16 mm, inner diameter: 8 mm), a 14 mm KTPO/C disk electrode as DE, and a KTP/C reference pin. Experiments included tests with pristine and preconditioned KTPO/C DE (preconditioning: see above). The wet film thickness of the KVP/C WE for the full cell setups was reduced to 100 µm to bypass a possible capacity limitation of the full cell caused by the limited areal capacity of the KTPO/C electrode. As electrolyte, 300 µL 0.5 M $KPF_6$ in EC:PC (1:1 by volume) was used, soaked in a Whatman GF/C separator with a diameter of 18 mm. The voltage window was set to 0.8–3.7 V in the full-cell setup with a preconditioned KTPO/C DE, while it was 0.6–3.8 V with an unconditioned KTPO/C DE. Galvanostatic charging (CCCV) with a CV step was performed at a Biologic SP-200 (Biologic, France). The C-rate test was performed at the following C-rates: C/20, C/10, C/5, C/2, and 1C (1C = 106 mA/g). All stated capacities refer to the composite mass of the KVP/C WE and not the active material content.


### Acknowledgments

This work contributes to the research performed at CELEST (Center of Electrochemical Energy Storage Ulm-Karlsruhe) and was funded by the Deutsche Forschungsgemeinschaft (DFG, German Research Foundation) under Germany's Excellence Strategy – EXC 2154 – Project number 390874152. The authors are grateful for the ICP-OES measurements, performed by Dr. Thomas Bergfeldt (IAM-AWP at KIT).

Open Access funding enabled and organized by Projekt DEAL.

### Funding

This study was supported by Deutsche Forschungsgemeinschaft (390874152).


### Conflicts of Interest

The authors declare no conflicts of interest.

### Data Availability Statement

The data that support the findings of this study are openly available in Zenodo at https://doi.org/10.5281/zenodo.21164078.

### References


1. IEA 2024, *Global Critical Minerals Outlook 2024* (IEA).

2. C. Vaalma, D. Buchholz, M. Weil, and S. Passerini, "A Cost and Resource Analysis of Sodium-Ion Batteries," *Nature Reviews Materials* 3, no. 4 (2018): 18013, https://doi.org/10.1038/natrevmats.2018.13.

3. F. Jeschull, E. Kataev, I. Panasenko, C. Njel, R. Félix, and J. Maibach, "Why Half-Cell Samples Provide Limited Insight Into the Aging Mechanisms of Potassium Batteries," *Advanced Energy Materials* 15, no. 6 (2025): 2403811, https://doi.org/10.1002/aenm.202403811.

4. S. Dhir, S. Wheeler, I. Capone, and M. Pasta, "Outlook on K-Ion Batteries," *Chem* 6, no. 10 (2020): 2442, https://doi.org/10.1016/j.chempr.2020.08.012.

5. S. Komaba, T. Hasegawa, M. Dahbi, and K. Kubota, "Potassium Intercalation Into Graphite to Realize High-Voltage/High-Power Potassium-Ion Batteries and Potassium-Ion Capacitors," *Electrochemistry Communications* 60 (2015): 172, https://doi.org/10.1016/j.elecom.2015.09.002.

6. J. Zhao, X. Zou, Y. Zhu, Y. Xu, and C. Wang, "Electrochemical Intercalation of Potassium Into Graphite," *Advanced Functional Materials* 26, no. 44 (2016): 8103, https://doi.org/10.1002/adfm.201602248.

7. B. Jagger, J. Aspinall, S. Kotakadi, J. Cattermull, S. Dhir, and M. Pasta, "Potassium Alloy Reference Electrodes for Potassium-Ion Batteries: The K-in and K-Bi Systems," *ACS Materials Letters* 6, no. 10 (2024): 4498, https://doi.org/10.1021/acsmaterialslett.4c01219.

8. T. Hosaka, S. Muratsubaki, K. Kubota, H. Onuma, and S. Komaba, "Potassium Metal as Reliable Reference Electrodes of Nonaqueous Potassium Cells," *Journal of Physical Chemistry Letters* 10, no. 12 (2019): 3296, https://doi.org/10.1021/acs.jpclett.9b00711.

9. I. Panasenko, M. Bäuerle, and F. Jeschull, "How Reference Electrodes Improve Our Understanding of Degradation Processes in Half and Full Cell Potassium-Ion Battery Setups," *Electrochimica Acta* 513 (2025): 145551, https://doi.org/10.1016/j.electacta.2024.145551.

10. E. C. Cengiz, J. Rizell, M. Sadd, A. Matic, and N. Mozhzhukhina, "Review—Reference Electrodes in Li-Ion and Next Generation Batteries: Correct Potential Assessment, Applications and Practices,"

*Journal of the Electrochemical Society* 168, no. 12 (2021): 120539, https://doi.org/10.1149/1945-7111/ac429b.

11. R. Nölle, K. Beltrop, F. Holtstiege, J. Kasnatscheew, T. Placke, and M. Winter, "A Reality Check and Tutorial on Electrochemical Characterization of Battery Cell Materials: How to Choose the Appropriate Cell Setup," *Materials Today* 32 (2020): 131, https://doi.org/10.1016/j.mattod.2019.07.002.

12. L. Wildersinn, D. Stottmeister, F. Jeschull, A. Gross, and A. Hofmann, "Decomposition of Binary Mixtures of DMC/EC, EMC/EC, and DEC/EC on Potassium Surfaces; GC, XPS, and Calculation," *ACS Applied Materials & Interfaces* 17, no. 6 (2025): 10055, https://doi.org/10.1021/acsami.4c17461.

13. L. Caracciolo, L. Madec, G. Gachot, and H. Martinez, "Impact of the Salt Anion on K Metal Reactivity in EC/DEC Studied Using GC and XPS Analysis," *ACS Applied Materials & Interfaces* 13, no. 48 (2021): 57505, https://doi.org/10.1021/acsami.1c19537.

14. S. Xing, A. Khudyshkina, U.-C. Rauska, et al., "Degradation of Styrene-Poly(ethylene Oxide)-Based Block Copolymer Electrolytes at the Na and K Negative Electrode Studied by Microcalorimetry and Impedance Spectroscopy," *Journal of the Electrochemical Society* 171, no. 4 (2024): 040516, https://doi.org/10.1149/1945-7111/ad3b72.

15. T. Hosaka, T. Fukabori, T. Matsuyama, R. Tatara, K. Kubota, and S. Komaba, "1,3,2-Dioxathiolane 2,2-Dioxide as an Electrolyte Additive for K-Metal Cells," *ACS Energy Letters* 6, no. 10 (2021): 3643, https://doi.org/10.1021/acsenergylett.1c01238.

16. K. Kubota, M. Dahbi, T. Hosaka, S. Kumakura, and S. Komaba, "Towards K-Ion and Na-Ion Batteries as "Beyond Li-Ion"," *Chemical Record* 18, no. 4 (2018): 459, https://doi.org/10.1002/tcr.201700057.

17. F. La Mantia, C. D. Wessells, H. D. Deshazer, and Y. Cui, "Reliable Reference Electrodes for Lithium-Ion Batteries," *Electrochemistry Communications* 31 (2013): 141, https://doi.org/10.1016/j.elecom.2013.03.015.

18. J. Costard, M. Ender, M. Weiss, and E. Ivers-Tiffée, "Three-Electrode Setups for Lithium-Ion Batteries," *Journal of the Electrochemical Society* 164, no. 2 (2016): A80, https://doi.org/10.1149/2.0241702jes.

19. N. Voronina, J. H. Jo, A. Konarov, J. Kim, and S. T. Myung, "$KTi_2(PO_4)_3$ Electrode With a Long Cycling Stability for Potassium-Ion Batteries," *Small* 16, no. 20 (2020): 2001090, https://doi.org/10.1002/smll.202001090.

20. J. Han, Y. Niu, S. J. Bao, Y. N. Yu, S. Y. Lu, and M. Xu, "Nanocubic $KTi_2(PO_4)_3$ Electrodes for Potassium-Ion Batteries," *Chemical Communications* 52, no. 78 (2016): 11661, https://doi.org/10.1039/c6cc06177j.

21. Z. Wei, D. Wang, M. Li, et al., "Fabrication of Hierarchical Potassium Titanium Phosphate Spheroids: A Host Material for Sodium-Ion and Potassium-Ion Storage," *Advanced Energy Materials* 8, no. 27 (2018): 1801102, https://doi.org/10.1002/aenm.201801102.

22. J. Hwang, S. Zhang, S. Ko, et al., "Reliable Evaluation of Na-Ion Battery Materials: Eliminating Na-Metal Distortions," *Advanced Energy Materials* (2026): e71044, https://doi.org/10.1002/aenm.71044.

23. W. M. Dose, M. J. Piernas-Muñoz, V. A. Maroni, S. E. Trask, I. Bloom, and C. S. Johnson, "Capacity Fade in High Energy Silicon-Graphite Electrodes for Lithium-Ion Batteries," *Chemical Communications* 54, no. 29 (2018): 3586, https://doi.org/10.1039/C8CC00456K.

24. W. M. Dose, V. A. Maroni, M. J. Piernas-Muñoz, S. E. Trask, I. Bloom, and C. S. Johnson, "Assessment of Li-Inventory in Cycled Si-Graphite Anodes Using $LiFePO_4$ as a Diagnostic Cathode," *Journal of the Electrochemical Society* 165, no. 10 (2018): A2389, https://doi.org/10.1149/2.1271810jes.

25. R. Zhang, J. Huang, W. Deng, et al., "Safe, Low-Cost, Fast-Kinetics and Low-Strain Inorganic-Open-Framework Anode for Potassium-Ion Batteries," *Angewandte Chemie International Edition* 58, no. 46 (2019): 16474, https://doi.org/10.1002/anie.201909202.

26. P. R. Kumar, K. Kubota, D. Igarashi, and S. Komaba, "Enhanced Electrochemical Properties of KTiOPO4–rGO Negative Electrode for Sodium and Potassium Ion Batteries," *Journal of Physical Chemistry C* 125, no. 45 (2021): 24823, https://doi.org/10.1021/acs.jpcc.1c08339.

27. C. Zhang and L. Zhou, "Potassium-Ion Battery Cathode—polyanionic Compounds," in *Electrochemical Potassium Storage - Principles, Materials and Technological Development*, ed. Y. Xu (WOODHEAD Publishing, 2025).

28. M. Li, C. Wang, C. Wang, et al., "10 Years Development of Potassium-Ion Batteries," *Advanced Materials* 37 (2025): 2416717, https://doi.org/10.1002/adma.202416717.

29. H. Huang, X. Wu, Y. Gao, et al., "Polyanionic Cathode Materials: A Comparison Between Na-Ion and K-Ion Batteries," *Advanced Energy Materials* 14, no. 14 (2024): 2304251, https://doi.org/10.1002/aenm.202304251.

30. A. Heyn, C. Röder, H. Geßwein, et al., "Hierarchical Microstructured $K_3V_2(PO_4)_3$/C-Composite Electrode for Potassium-Ion-Batteries Through Scalable Spray-Drying Approach," *ChemSusChem* 18, no. 16 (2025): e202501111, https://doi.org/10.1002/cssc.202501111.

31. E. S. Lunezheva, B. A. Maksimov, and O. K. Mel'Nikov, "Structure Cristalline De $KTi_2(PO_4)_3$; $KTi_2(PO_4)_3$ Crystal Structure," *Kristallografiâ* 34, no. 5 (1989): 1119.

32. A. Leclaire, A. Benmoussa, M. M. Borel, A. Grandin, and B. Raveau, "$K_2{-}xTi_2(PO_4)_3$ With $0 \leq x \leq 0.5$: A Mixed-Valence Nonstoichiometric Titanophosphate With the Langbeinite Structure," *Journal of Solid State Chemistry* 78, no. 2 (1989): 227, https://doi.org/10.1016/0022-4596(89)90101-1.

33. M. Häringer, "Synthese Und Hochskalierung Hierarchisch Strukturierter NASICON-Materialien Als Kathodenmaterial für Natrium-Ionen-Batterien," (2023).

34. S. T. Norberg, P. A. Thomas, and M. G. Tucker, "A Neutron Total Scattering Study of Local Coordination in $KTiOPO_4$ From Room Temperature to 900 °C," *Journal of Physics: Condensed Matter* 23, no. 17 (2011): 175401, https://doi.org/10.1088/0953-8984/23/17/175401.

35. M. Sakao, N. Kijima, J. Akimoto, and T. Okutani, "Synthesis, Crystal Structure, and Electrochemical Properties of Hollandite-Type $K0.008TiO_2$," *Solid State Ionics* 225 (2012): 502, https://doi.org/10.1016/j.ssi.2011.11.023.

36. M. Häringer, H. Geßwein, N. Bohn, H. Ehrenberg, and J. R. Binder, "Influence of Process Parameters on the Electrochemical Properties of Hierarchically Structured $Na_3V_2(PO_4)_3$/C Composites," *ChemElectroChem* 11, no. 3 (2024): e202300401, https://doi.org/10.1002/celc.202300401.

37. Y. Qi, J. Li, W. Zhong, S. Bao, and M. Xu, "$KTiOPO_4$: A Long-Life, High-Rate and Low-Temperature-Workable Host for Na/K-Ion Batteries," *Chemical Engineering Journal* 417 (2021): 128159, https://doi.org/10.1016/j.cej.2020.128159.

38. S. Huang and G. Xu, "$KTi_2(PO_4)_3$ Nanoparticles Wrapped in 3D RGO as Enhanced Electrode for Potassium-Ion Batteries," *Materials Letters* 361 (2024): 136156, https://doi.org/10.1016/j.matlet.2024.136156.

39. W. Zhang, Y. Liu, and Z. Guo, "Approaching High-Performance Potassium-Ion Batteries via Advanced Design Strategies and Engineering," *Science Advances* 5, no. 5 (2019): eaav7412, https://doi.org/10.1126/sciadv.aav7412.

40. Y. Xu, M. Titirici, J. Chen, et al., "2023 Roadmap for Potassium-Ion Batteries," *Journal of Physics: Energy* 5, no. 2 (2023): 021502, https://doi.org/10.1088/2515-7655/acbf76.

41. Y. Liu, Z. Tai, J. Zhang, et al., "Boosting Potassium-Ion Batteries by Few-Layered Composite Anodes Prepared via Solution-Triggered One-Step Shear Exfoliation," *Nature Communications* 9, no. 1 (2018): 3645, https://doi.org/10.1038/s41467-018-05786-1.

42. S. E. Lee and M. H. Tang, "Reliable Reference Electrodes for Nonaqueous Sodium-Ion Batteries," *Journal of the Electrochemical Society* 166, no. 14 (2019): A3260, https://doi.org/10.1149/2.0401914jes.

43. F. Linsenmann, D. Pritzl, and H. A. Gasteiger, "A Reference Electrode for In Situ Impedance Measurements in Sodium-Ion Batteries," *Journal of the Electrochemical Society* 166, no. 15 (2019): A3668, https://doi.org/10.1149/2.0741915jes.

44. P. W. Ruch, D. Cericola, M. Hahn, R. Kotz, and A. Wokaun, "On the use of Activated Carbon as a Quasi-Reference Electrode in Non-Aqueous Electrolyte Solutions," *Journal of Electroanalytical Chemistry* 636, no. 1-2 (2009): 128–131, https://doi.org/10.1016/j.jelechem.2009.09.007.

45. C. Bünzli, H. Kaiser, and P. Novák, "Important Aspects for Reliable Electrochemical Impedance Spectroscopy Measurements of Li-Ion Battery Electrodes," *Journal of the Electrochemical Society* 162, no. 1 (2014): A218, https://doi.org/10.1149/2.1061501jes.

46. J. Dong, Y. Dong, X. Cheng, et al., "Optimized Porous $KTi_2(PO_4)_3$@N-Doped Carbon Electrode for Enhanced Sodium/Potassium-Storage and Accelerated Activation Process," *ACS Applied Materials & Interfaces* 17, no. 12 (2025): 18319, https://doi.org/10.1021/acsami.4c22245.

47. J. Rizell, W. Chrobak, N. Mozhzhukhina, S. Xiong, and A. Matic, "Electrochemical Signatures of Potassium Plating and Stripping," *Journal of the Electrochemical Society* 171, no. 2 (2024): 020517, https://doi.org/10.1149/1945-7111/ad2593.

48. K.-H. Chen, K. N. Wood, E. Kazyak, et al., "Dead Lithium: Mass Transport Effects on Voltage, Capacity, and Failure of Lithium Metal Anodes," *Journal of Materials Chemistry A* 5, no. 23 (2017): 11671, https://doi.org/10.1039/C7TA00371D.

49. K. Xu, "Nonaqueous Liquid Electrolytes for Lithium-Based Rechargeable Batteries," *Chemical Reviews* 104, no. 10 (2004): 4303, https://doi.org/10.1021/cr030203g.

50. L. Ling, X. Wang, M. Zhou, et al., "Carbon-Coated Flower-Like $TiO_2$ Nanosphere as an Ultrastable Anode Material for Potassium-Ion Batteries: Structure Design and Mechanism Study," *ACS Applied Energy Materials* 5, no. 12 (2022): 15586, https://doi.org/10.1021/acsaem.2c03171.

51. S. Zheng, S. Cheng, S. Xiao, et al., "Partial Replacement of K by Rb to Improve Electrochemical Performance of $K_3V_2(PO_4)_3$ Cathode Material for Potassium-Ion Batteries," *Journal of Alloys and Compounds* 815 (2020): 152379, https://doi.org/10.1016/j.jallcom.2019.152379.

52. H.-X. Kuai, J.-F. Lu, X.-Y. Lv, S. Jing, Y.-F. Long, and Y.-X. Wen, "High-Performance, Three-Dimensional and Porous $K_3V_2(PO_4)_3$/C Cathode Material for Potassium-Ion Batteries," *Ionics* 28, no. 8 (2022): 3817, https://doi.org/10.1007/s11581-022-04612-5.

53. J. Han, G. N. Li, F. Liu, et al., "Investigation of $K_3V_2(PO_4)_3$/C Nanocomposites as High-Potential Cathode Materials for Potassium-Ion Batteries," *Chemical Communications* 53, no. 11 (2017): 1805–1808, https://doi.org/10.1039/c6cc10065a.

## Supporting Information

Additional supporting information can be found online in the Supporting Information section.